THE JOURNAL OF PHYSICAL CHEMISTRY C

Article

Cite This: J. Phys. Chem. C 2018, 122, 6209−6216

pubs.acs.org/JPCC

# Tunable Electronic and Optical Properties of Monolayer and Multilayer Janus MoSSe as a Photocatalyst for Solar Water Splitting: A First-Principles Study

Zhaoyong Guan,*[,†,‡,§] Shuang Ni,[∥] and Shuanglin Hu[†]

[†]Institute of Nuclear Physics and Chemistry, China Academy of Engineering Physics, Mianyang, Sichuan 621900, P. R. China

[‡]Department of Physics and State Key Laboratory of Low-Dimensional Quantum Physics, Tsinghua University, Beijing 100084, P. R. China

[§]Department of Physics, Tsinghua University, Beijing 100084, P. R. China

[∥]Research Center of Laser Fusion, China Academy of Engineering Physics. Mianyang, Sichuan 621900, P. R. China

Supporting Information

**ABSTRACT:** Recently, novel two-dimensional materials for solar water splitting have drawn enormous research attention for the interesting tunable electronic and optical properties. We investigate the geometry, electronic, and optical properties of the monolayer (ML) and multilayer Janus MoSSe with the first-principles calculations. We find that the ML Janus MoSSe is a semiconductor with a direct band gap of 2.14 eV, which is suitable for absorbing visual light efficiently. It also holds an appropriate band edge alignment with the water redox potentials. The biaxial strain could effectively modulate the electronic and optical properties of the ML MoSSe, from a direct semiconductor to the indirect one, even to be metal. As for the bilayer (BL) MoSSe, the stacking order could effectively affect the electronic, optical, and redox properties. The most stable stacking order is the A′B type, followed by the AA′, AA-SeSe, AA-SS, and AA-SSe stacking faults. For the BL MoSSe, they are all indirect semiconductors. The indirect band gap of the multilayer MoSSe decreases monotonously as the number of layers increases, maybe due to the quantum confinement effect and interaction between the layers. The appropriate optical and band alignment with the water redox potentials together with the rich modulation methods imply that MoSSe could be used as an efficient photocatalysist for the water splitting.

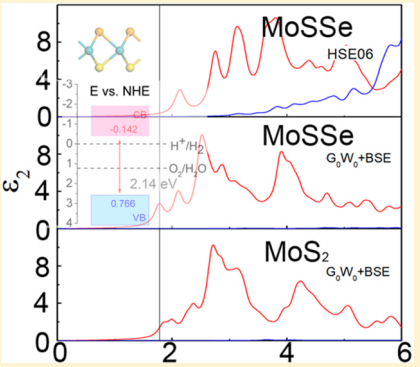


## 1. INTRODUCTION

The energy crisis caused by the oil shortage makes people worry about the limitness of the fossil energy. This promotes the world to develop renewable and environment-friendly energy resources. As one of the representatives of the clean and limitless energies, solar energy is low cost and widely spread in the world.[1] The use of photocatalytic water splitting for hydrogen may be the best way for solar energy conversion and storage.[2] In view of the water and solar energy with abundant reserves, utilizing semiconductors to split water to produce hydrogen is an effective and credible way of hydrogen fuel generation.[1−4] Therefore, synthesizing and developing an efficient and environment-friendly photocatalyst with good catalytic activity for hydrogen production is always quite important and urgent.[4] There have been much research proposing that the two-dimensional (2D) transition metal dichalcogenide (TMD) family is among the most promising materials for photocatalyst of water splitting.[5] There are many inherent advantages as photocatalyst[2,6−18] for 2D materials. 2D materials have ideally maximal specific surface area per amount of material,[19,20] and they could promote the photogenerated electrons and holes to migrate to the reaction interfaces,[5,8,11,19] posing tunable enormous electronic and optical properties.[19,21]

Recently, ML Janus MoSSe has been successfully synthesized and characterized by the Zhang[22] and Lou groups.[23] As shown in Figure 1a,b, one side of the Janus MoSSe are S atoms and the other side are Se atoms. The Mo atom layer is sandwiched between S and Se layers. The geometry of ML Janus MoSSe is thus different from $MoS_2$ and $MoSe_2$,[15,24] and would show new properties that $MoS_2$ or $MoSe_2$ may not hold. For example, several exotic properties of MoSSe have been studied by theoretical calculations. Cheng et.al. have investigated the structural stability and spin−orbit-induced spin splitting in the monolayer MoXY.[25] Dong et.al. have pointed out that ML and multilayer Janus MoXY show a strong piezoelectric effect.[26] It is well-known that the excitonic effect also plays an important role in the TMD materials after the pioneering work of Cheiwchanchamnangij[27] and Ramasubramaniam et al.[28] However, there is still little work on the electronic, optical, and redox properties of the ML and multilayer Janus MoSSe, used as photocatalyst for the water splitting.

**Received:** January 9, 2018
**Revised:** February 10, 2018
**Published:** March 5, 2018

ACS Publications © 2018 American Chemical Society



DOI: 10.1021/acs.jpcc.8b00257
J. Phys. Chem. C 2018, 122, 6209−6216

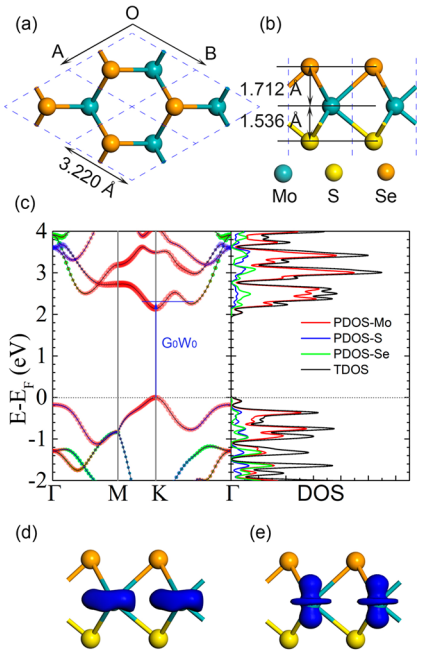


**Figure 1.** (a) Top and (b) side views of the optimized geometry of ML Janus MoSSe. The cyan, yellow, and orange balls represent Mo, S, and Se atoms, respectively. (c) Band structure and DOS of the ML MoSSe. The red, blue, and green dots present the projected band and DOS from the Mo, S, and Se atoms, respectively. The size of the dots in the band indicates the weight of contributions. The Fermi level ($E_F$) was set to 0 eV. (d, e) Charge densities of the ML MoSSe: (d) VBM and (e) CBM. The Γ, M, and K *k*-points are (0, 0, 0), (0, 1/2, 0), and (1/3, 1/3, 0), respectively.

In this article, by using the first-principles method with van der Waals interactions,[29−34] we investigate the geometric, electronic, and optical properties of mono- and multi-layer Janus MoSSe. We study the electronic and optical properties using a hybrid functional[35,36] and then further using the quasi-particle $G_0W_0$[37−42] and the Bethe−Salpeter equation (BSE)[43,44] to account for the optical properties and the excitonic effect. We find ML MoSSe is a semiconductor with a direct band gap of 2.14 eV with the HSE06 functional[35,36] for the first time. The conduction band minimum (CBM) is located above the reduction potential of $H^+/H_2$, whereas the valence band maximum (VBM) is well below the oxidation potential of $O_2/H_2O$, indicating that the Janus MoSSe is a potential photocatalyst for water splitting. The band gap, band alignment with water redox potentials, and optical properties of ML MoSSe under biaxial strains are also systematically investigated. When the ML MoSSe is increased to the bilayer, the stacking orders, with closely related corresponding geometries, electronic properties, and work functions, are also studied. At last, we investigate the relationship between the electronic properties and the number of MoSSe layers.

## 2. COMPUTATIONAL DETAILS

The calculations on the MoSSe are performed by using the plane-wave basis Vienna Ab initio Simulation Package (VASP) code,[45,46] based on the density functional theory under the generalized gradient approximation (GGA) with the Perdew−Burke−Ernzerhof (PBE).[47] In view of the disadvantage of the PBE functional in underestimating the band gap of the semiconductors, a more reliable Heyd−Scuseria−Ernzerhof (HSE06)[35,36] screened hybrid functional is adopted to calculate the electronic properties, respectively. The optical properties of the Janus MoSSe are calculated by HSE06 and HSE06+$G_0W_0$+BSE, respectively. In order to more accurately describe the weak van der Waals (vdW) interactions, van der Waals correction, including the DFT-D2 developed by Grimme,[29] optB86b,[30−32] and the method of Tkatchenko and Scheffler (DFT-TS)[33,34] are also adopted. In this work, DFT-D2, optB86b, and DFT-TS provide the consistent result. Thus, we mainly use DFT-D2,[29] which could provide a good description of long-range vdW interactions of low dimensional materials[47,48] to calculate the electronic and optical properties of MoSSe. The calculated interlayer distance for BL graphene is 3.25 Å, and the binding energy per carbon atom is about −25 meV, which is consistent with the previous studies.[49−51] The vacuum space in the *z*-direction is set as large as 20 Å to avoid the interactions between the periodic images. The kinetic energy cutoff for plane waves is set as 400 eV, and the geometries are fully relaxed until energy is converged to $10^{-6}$ eV. Monkhorst−Pack[52] *k*-grids with 9 × 9 × 1, 11 × 11 × 1, and 16 × 16 × 1 are adopted for Brillouin zone integration for geometry optimization and energy and density of states (DOS) computation, respectively. Also, 90 uniform *k*-points along the high-symmetry special *k*-paths are used to obtain the band structure. Optimizing geometry without any symmetry restriction is performed by using the conjugate gradient scheme until the force acting on every atom is less than 1 meV/Å.

In order to investigate the optical properties, the imaginary parts of the frequency dependent complex dielectric function ($\varepsilon_2(\omega)$) are also calculated. $\varepsilon_2(\omega)$ is calculated using the following equation[53]

$$\varepsilon^{(2)}_{\alpha\beta}(\omega) = \frac{4\pi^2 e^2}{\Omega} \lim_{q\to 0} \frac{1}{q^2} \sum_{c,v,k} 2\omega_k \delta(\varepsilon_{ck} - \varepsilon_{vk} - \omega) \times \langle u_{ck} + e_{\alpha q}|u_{vk}\rangle\langle u_{ck} + e_{\beta q}|u_{vk}\rangle^*$$

where the indices *c* and *v* present conduction and valence band (CB and VB) states, respectively, and $u_{ck}$ stands for the cell periodic part of the orbitals at the *k*-point. This formula is widely used to calculate the optical properties of materials.[48] When the BSE is taken into consideration, the electron−hole interactions are included in the electronic description. BSE introduces higher order interaction diagrams and improves the electronic description systematically on top of GW.[43,44]

## 3. RESULTS AND DISCUSSION

**3.1. Geometry of the ML Janus MoSSe.** We first optimize the geometry of ML Janus MoSSe, as shown in Figure 1a,b. The corresponding optimized lattice parameter is $a = b =$ 3.220 Å, which is slightly larger than $MoS_2$ (3.170 Å) but smaller than $MoSe_2$ (3.470 Å), and it is consistent with the previous results.[22−25] This lattice could be viewed as the compromise of $MoS_2$ and $MoSe_2$. The vertical distance between Mo and S and Mo and Se is 1.536 and 1.712 Å, respectively, which is smaller than the corresponding value in $MoS_2$ (1.564 Å) but bigger than that in $MoSe_2$ (1.670 Å). The corresponding bond lengths of Mo−Se and Mo−S are 2.527 and 2.412 Å, respectively. From the optimized geometries, we can find that ML Janus MoSSe breaks out-of-plane structure symmetry, as one side are all S atoms, while the other are all Se atoms, respectively.

**3.2. Electronic Structure, Band Alignment, and Optical Properties.** In the above section, we have optimized



DOI: 10.1021/acs.jpcc.8b00257
J. Phys. Chem. C 2018, 122, 6209−6216

the geometry of the ML MoSSe, and we now focus on the electronic properties of the ML MoSSe. The band structure and DOS of ML MoSSe are calculated by the HSE06 functional, shown in Figure 1c,d, respectively. From the band structure, we can find that the ML MoSSe is a semiconductor with a direct band gap of 2.14 eV, which means ML MoSSe would be an excellent light harvesting material. Both VBM and CBM are located at the K point in the irreducible Brillouin zone, indicating that the electrons could be directly photoexcited from the VBM to the CBM, which is feasible for the generation of photoexcited electrons and holes.

In order to further analyze the electronic properties of the ML MoSSe, the projected DOS (PDOS) is also calculated, shown in Figure 1d. From the PDOS, we can find that the states near the VBM and CBM are mainly contributed by the Mo atoms. The VBM is mainly contributed by the $d_{x^2-y^2}$ and $d_{xy}$ orbitals of the Mo atoms, while the CBM is mainly contributed by the $d_{z^2}$ orbital of the Mo atoms, shown in Figure S1 in the Supporting Information. This is also consistent with the distribution of the charge densities of the VBM and CBM, shown in Figure 1d and e, respectively.

On considering the band gap, ML MoSSe should be an appropriate light harvesting material. In order to investigate the catalytic properties, the band alignment with the oxidation and reduction potentials of splitting water is needed to be further investigated. We first calculate the vacuum energy level by plotting the *xy*-plane averaged electrostatic potential of ML MoSSe. The VBM and CBM are subtracted by the vacuum energy level. The oxidation potential of $O_2/H_2O$ lies at −5.670 eV and the reduction potential of $H^+/H_2$ lies at −4.440 eV relative to the vacuum level, shown in the work of Wei et al.[54] Then, if one aligns the levels again with respect to the standard hydrogen electrode (NHE) potential, the reduction potential of $H^+/H_2$ is thus set to 0 eV, and the oxidation potential of $O_2/H_2O$ is set to 1.230 eV. For ML MoSSe, the calculated energy level of VBM is −6.436 eV, which is 0.766 eV below the oxidation potential $O_2/H_2O$. CBM is −4.298 eV, which is 0.142 eV above the $H^+/H_2$, shown in Figure 2a. This means that the water oxidation and reduction reactions should be thermodynamically feasible for ML MoSSe with a zero or small additional voltage.

To be an excellent photocatalyst, the suitable band gap and band edge positions are very important, and another important requirement is that the photocatalytic materials could efficiently absorb the sunlight, especially visible light. Therefore, we also calculate the imaginary part of the frequency dependent complex dielectric function ($\varepsilon_2(\omega)$) of MoSSe, as shown in Figure 2b,c. On the basis of the structural anisotropy, the corresponding $\varepsilon_2$ is distributed into three parts: $\varepsilon_2$ along the *xx*, *yy*, and *zz* directions, with $\varepsilon_2^{xx} = \varepsilon_2^{yy} \neq \varepsilon_2^{zz}$, and a similar relation also holds in the *g*-$C_2N$ layer.[48] The $\varepsilon_2$ is mainly contributed by $\varepsilon_2^{xx}$ and $\varepsilon_2^{yy}$ components, while the $\varepsilon_2^{zz}$ component only makes little contribution. The first peak locates at 2.15 eV, similar to the band gap (2.14 eV) of the ML MoSSe, indicating that photoexcited electrons can directly transitioned from the VBM to the CBM. The second and third peaks locate at 2.77 and 3.15 eV. For the visible light range (corresponding to the photon energy between 1.63 and 3.12 eV), there is an obvious absorption for the ML MoSSe, which demonstrates that the ML MoSSe could be a light harvesting material. The visual light absorption is mainly composed of in-plane contributions ($\varepsilon_2^{xx}$ and $\varepsilon_2^{yy}$ components). As 2D materials, TMDs are proven to show strong excitonic effects, having an influence on their optical properties.[27,28] We thus also use quasiparticle (QP) plus optical response including electron−electron interactions and excitonic contributions with the GW plus BSE approach.[40,41] We use HSE06+$G_0W_0$+BSE to calculate the $\varepsilon_2(\omega)$[37−43] of MoSSe and $MoS_2$. As shown in Figure 2b, the first peak of MoSSe locates at 2.13 eV, smaller than the band gap (2.14 eV) calculated by HSE06. The second peak is also transferred to 2.76 eV. The band gap of MoSSe calculated by $G_0W_0$ is 2.30 eV, smaller than 2.41 eV of $MoS_2$. For $\varepsilon_2$ calculated by $G_0W_0$+BSE, the first peak of MoSSe is located at 1.77 eV, which is smaller than 1.87 eV of $MoS_2$, and this may be caused by the smaller band gap of ML MoSSe.

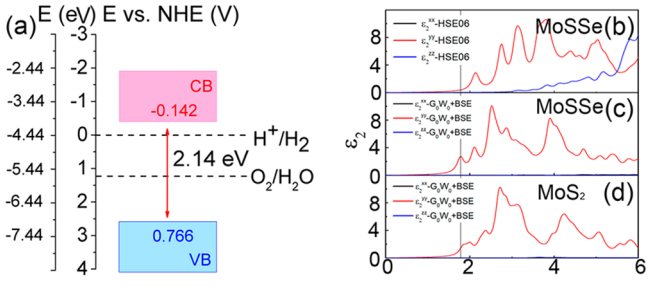


**Figure 2.** (a) Band edge positions and (b) the imaginary part of the dielectric function $\varepsilon_2^{xx}$, $\varepsilon_2^{yy}$, and $\varepsilon_2^{zz}$ corresponding to the components along the *X*, *Y*, and *Z* directions, respectively. The black, red, and blue lines represent the imaginary components in the *X*, *Y*, and *Z* directions of (b) monolayer MoSSe with HSE06, (c) MoSSe, and (d) $MoS_2$ calculated by $G_0W_0$ plus BSE based on HSE06 wave functions, respectively.

**3.3. Effect of the Biaxial Strain.** For 2D materials, they are usually synthesized and characterized on many different kinds of substrates.[27,38,47,48,51,55−59] Considering the lattice match between 2D materials and substrate, it is demanded to examine the strain effect on their properties. Moreover, the strain is often used as an effective way of modulating the properties of the materials by changing the bond strength.[60−62] Thus, it is quite necessary to investigate the electronic properties of 2D materials placed on the substrates (vdW structures).[58,59,62] To simplify this issue, we first study the effect of the biaxial strains ($\varepsilon$) on the electronic properties of the ML MoSSe, shown in Figure 3. The biaxial strain could transform the ML MoSSe from a direct to an indirect gap semiconductor, and a similar phenomenon also appears in the ML $MoS_2$.[60−64] When the compressive $\varepsilon$ monotonically increases, the band gap first increases and then decreases for changing the bond strength.[60] For the compressive biaxial strain $\varepsilon$ = −1%, the ML MoSSe is still a direct semiconductor with a band gap of 2.23 eV. As the compressive $\varepsilon$ is increased to −2%, the ML MoSSe undergoes a direct-to-indirect band gap transition, while the energy level of CBM (the midpoint along Γ−K symmetry lines, with $E_Q$ in short) is 0.06 eV lower than the K point ($E_K$). For $\varepsilon$ = −3 and −2%, the corresponding band gaps are 2.00 and 2.16 eV, as the energy difference between $E_K$ and $E_Q$ is increased to 0.48 eV from 0.06 eV, respectively. For $\varepsilon$ = −4 and −5%, the band gaps are 2.09 and 2.03 eV, respectively. When the compressive $\varepsilon$ is increased to −6%, the corresponding band gap is further decreased to 1.82 eV. The energy difference between $E_K$ and $E_Q$ is also increased to 1.13 eV. With the increasing compressive strain, the VBM composed of the $d_{x^2-y^2}$ and $d_{xy}$ orbitals of Mo atoms is still located at the K point, but the CBM composed of $d_{x^2-y^2}$ and $d_{z^2}$ orbitals of Mo atoms with the $p_y$ orbital of the Se


DOI: 10.1021/acs.jpcc.8b00257
J. Phys. Chem. C 2018, 122, 6209−6216

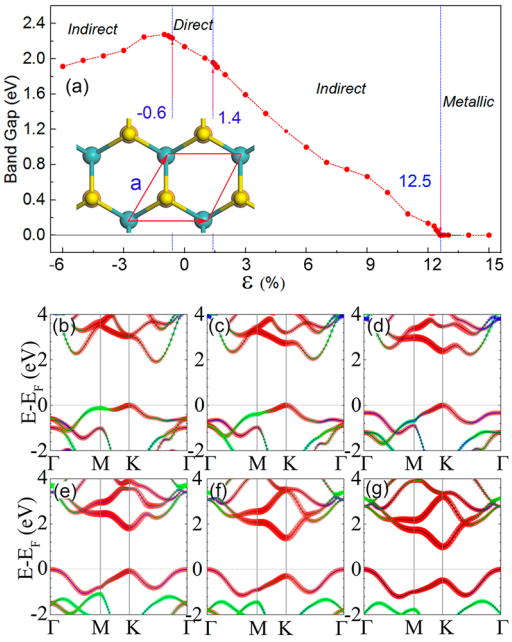


**Figure 3.** (a) The band gap of ML MoSSe calculated by HSE06 varies with the biaxial strains, ranging from −6 to 15%. The band structure of ML MoSSe under biaxial strains with (b) −6%, (c) −4%, (d) −2%, (e) 2%, (f) 4%, and (g) 6%. The sizes of the red, blue, and green dots present the weights of Mo, S, and Se atoms, respectively.

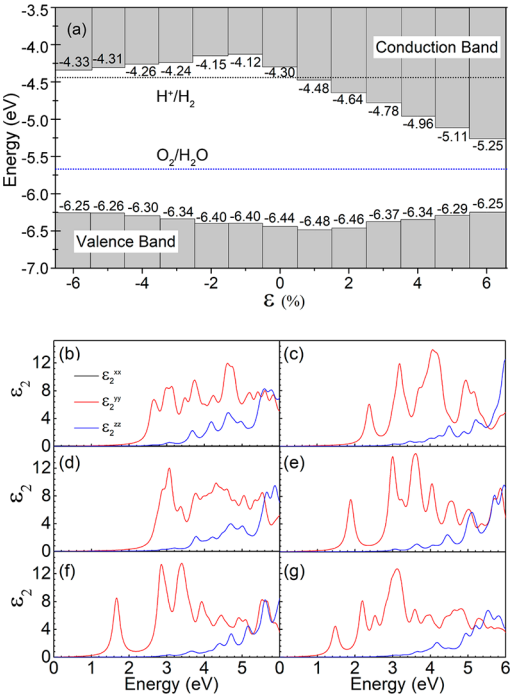


**Figure 4.** (a) The band alignment of ML MoSSe under biaxial strains. (b–g) Imaginary part of the dielectric function. The black, red, and blue lines represent the component in the *X*, *Y*, and *Z* direction of ML MoSSe with different biaxial strains calculated by HSE06, with (b) −6%, (c) −4%, (d) −2%, (e) 2%, (f) 4%, and (g) 6%, respectively.

atoms is transferred from the original K point to the midpoint along Γ−K symmetry lines.

As the tensile biaxial strain increases, the band gap of the ML MoSSe decreases. Except for the smaller $\varepsilon$ = 1%, the MoSSe is preserved to be a direct semiconductor. As the tensile strain goes on increasing ($\varepsilon$ > 1.5%, more details could be found in the Supporting Information), ML MoSSe transfers from a direct into an indirect gap semiconductor, which also appears in $MoS_2$.[60,62] The VBM composed of $d_{x^2-y^2}$ and $d_{xy}$ orbitals of Mo atoms also transfers from the original K point to the Γ point. However, the CBM composed of the $d_{z^2}$ orbital of the Mo atom is still located at the K point. As the strain further increases to 12.6%, the ML MoSSe transfers from semiconductor to metal. In a word, the ML MoSSe preserves a direct semiconductor for the smaller strains ($-0.6\% \le \varepsilon \le 1.5\%$), while ML MoSSe could transfer into the small indirect gap semiconductor and even metal for the larger biaxial tensile strains.

We also investigate the band alignment under biaxial strains from −6 to 6% (1% interval near the distance of the equilibrium), shown in Figure 4a, and the optical properties $\varepsilon_2$ are calculated and shown in Figure 4b–g, respectively. For the considered compressive biaxial strains, the VBM of ML MoSSe is always lower than the oxidation potential of $O_2/H_2O$ and the CBM is always higher than the reduction potential of $H^+/H_2$. Thus, the ML Janus MoSSe could produce $H_2$ and $O_2$ at the same time, under the smaller compressive biaxial strains ($\varepsilon$ < −6%). For the considered tensile biaxial strains ($\varepsilon$ > 1%), the VBM is always more negative than the oxidation potential of $O_2/H_2O$, while the CBM is always more negative than the reduction potential of $H^+/H_2O$. It indicates that ML MoSSe could only take part in the oxidation reaction, while the reduction reaction is energetically unfavorable.

Besides the band alignment, the optical properties of ML MoSSe are systematically investigated with the HSE06 functional, shown in Figure 4b–g. $\varepsilon_2$ is still mainly contributed by the $\varepsilon_2^{xx}$ and $\varepsilon_2^{yy}$ components, while the $\varepsilon_2^{zz}$ component implies it mainly absorbs the ultraviolet light. The first peak of $\varepsilon_2$ is blue-shifted under the biaxial strains from 0 to compressive −6%, while this peak is red-shifted from 0 to tensile 6%. In a word, the optical absorption of the ML MoSSe could be regulated by the biaxial strains, and the ML MoSSe still shows an obvious absorption of the visual light under the biaxial strains.

**3.4. Effect of the Stacking Order.** The bilayer MoSSe is the smallest MoSSe multilayer system stacked by the vdW interactions. It is interesting to know the following: (i) What are the electronic properties of the BL MoSSe? (ii) Are the electronic properties of BL MoSSe also closely related with the stacking configurations?

Moreover, the Janus MoSSe is usually synthesized with multilayers stacked together by the vdW interactions.[22,23] Therefore, the stacking induced modifications on the electronic and optical properties need to be systemically discussed. Taking bilayer $MoS_2$ as a reference,[65] five different high-symmetry stacking patterns—AA′, A′B, AA-SeSe, AA-SSe, and AA-SS—of BL MoSSe are considered, and the optimized geometries are shown in Figure 5a–e, respectively. The interlayer vertical distance of the plane of the Se and S (Se) atoms *d* is defined to describe the interaction between the MoSSe layers, as shown in Figure 5a. The corresponding distance and binding energies calculated by the DFT-D2, optB86b, and DFT-TS methods are shown in Table 1. From Table 1, we can find the A′B configuration with the smallest *d* = 3.123 Å calculated by DFT-D2, which is smaller than AA′ (3.145 Å) and AA-SeSe (3.743 Å), AA-SSe (3.807 Å), and AA-SS (3.806 Å), respectively. $E_b$ is defined as $E_b = E_{bilayer} - E_{monolayer} \times 2$, where $E_{bilayer}$ is the total energy of the relaxed bilayer MoSSe. The corresponding $E_b$ for the A′B configuration is −0.179 eV, while the corresponding


DOI: 10.1021/acs.jpcc.8b00257
J. Phys. Chem. C 2018, 122, 6209−6216

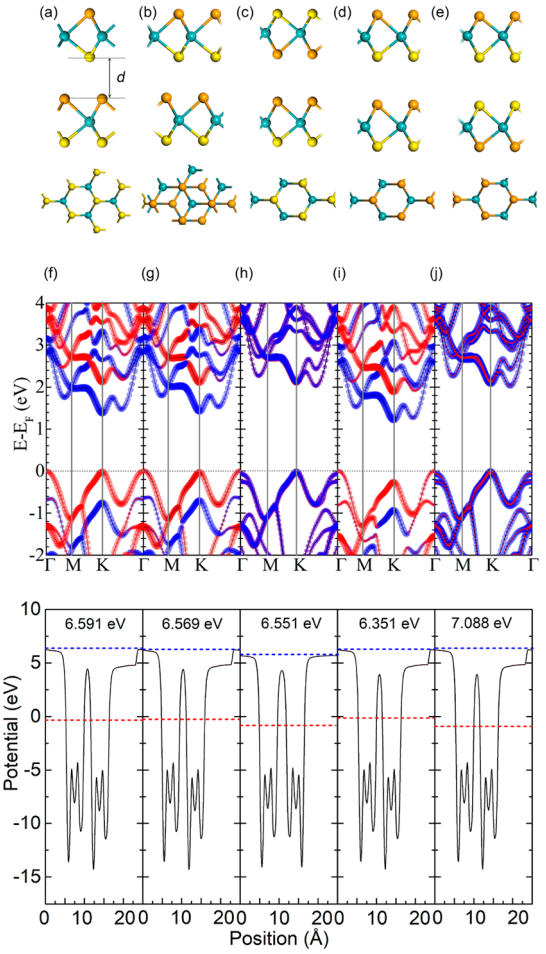


**Figure 5.** Optimized structures of BL MoSSe with stacking of (a) AA′, (b) A′B, (c) AA-SeSe, (d) AA-SSe, and (e) AA-SS. Parts f–j show the corresponding band structure calculated by HSE06, respectively. The red and blue lines with dots present the weights of the bottom and top MoSSe layers, respectively. The bottom shows the *xy*-averaged electrostatic potential of parts a–e, respectively. The red and blue dashed lines present the Fermi level and the vacuum potential, respectively.

**Table 1. Distance between Two Janus MoSSe Layers and Corresponding Binding Energy of the BL MoSSe with Different Stacking Orders Calculated by DFT-D2, optB86b, and TS, respectively**

| | DFT-D2 | | optB86b | | TS | |
|---|---|---|---|---|---|---|
| system | $d_0$ (Å) | $E_b$ (eV) | $d_0$ (Å) | $E_b$ (eV) | $d_0$ (Å) | $E_b$ (eV) |
| AA′ | 3.145 | −0.177 | 3.111 | −0.225 | 2.924 | −0.242 |
| A′B | 3.123 | −0.179 | 3.073 | −0.227 | 2.662 | −0.264 |
| AA-SeSe | 3.743 | −0.123 | 3.807 | −0.152 | 3.575 | −0.179 |
| AA-SSe | 3.807 | −0.107 | 3.708 | −0.151 | 3.497 | −0.176 |
| AA-SS | 3.806 | −0.123 | 3.807 | −0.152 | 3.574 | −0.172 |

values of AA′, AA-SSe, and AA-SeSe (AA-SS) are −0.177, −0.107, and −0.123 eV, respectively. Thus, the A′B configuration is the most stable structure, which is different from the $MoS_2$,[61,64,65] while the $E_b$ of $MoS_2$ and $MoSe_2$ with the most stable configuration are −0.074 and −0.107 eV, respectively.[65] Other optimized vdW-DF functionals (such as optB86b-vdW[30−32]) and self-consistent screening of the Tkatchenko–Scheffler method (DFT-TS[33]) are also adopted to investigate the BL MoSSe. The $E_b$ calculated by optB86b for the A′B configuration with the smallest distance (3.073 Å) is −0.227 eV, while the corresponding values of AA′, AA-SeSe, AA-SSe, and AA-SS are −0.225, −0.152, −0.151, and −0.152 eV, respectively. A similar trend is also shown in the DFT-TS results. The A′B configuration is the most stable within all three methods, and all results are collected in Table 1.

In terms of TMDs, the electronic properties are usually related with the stacking patterns.[55−61] For the BL MoSSe, the electronic properties are also dependent on the stacking orders. For the most stable A′B configuration, the VBM is located at the Γ point, while the CBM is located at the K point, suggesting it is an indirect semiconductor with a gap of 1.47 eV. For AA′ and AA-SSe, the VMB is located at the Γ point, while the CBM is still located at the K point, and the corresponding direct band gaps are 1.39 and 1.22 eV, respectively. Meanwhile, the VBM and CBM are distributed in the top and bottom layers, respectively. For AA-SeSe and AA-SS, the VBM is located at the K point, while the CBM is located at the midpoint along K–Γ symmetry lines. From ML to BL, MoSSe is transformed from a direct band gap semiconductor to an indirect one, which is predicted to be caused by the vdW interaction between the MoSSe layers, long-range Coulomb effects, and quantum confinement.[66−68]

Besides that, the DFT-D2 calculated band alignment of the BL MoSSe with the different stacking orders are compared with the water redox and reduction potential, shown in Table 2. For

**Table 2. Distance between Two Janus MoSSe Layers, Corresponding Binding Energy, Band Gap, and Band Alignment of the BL Janus MoSSe with Different Stacking Orders[a]**

| system | distance (Å) | $E_b$ (eV) | gap (eV) | VBM-Ev (eV) | CBM-Ev (eV) |
|---|---|---|---|---|---|
| AA′ | 3.145 | −0.177 | 1.39 | −6.35 | −4.97 |
| A′B | 3.123 | −0.179 | 1.47 | −6.43 | −5.24 |
| AA-SeSe | 3.743 | −0.123 | 2.11 | −6.64 | −4.54 |
| AA-SSe | 3.807 | −0.107 | 1.22 | −6.45 | −5.23 |
| AA-SS | 3.806 | −0.123 | 2.11 | −7.18 | −5.08 |

[a]The Ev stands for the energy level of the vacuum.

the most stable A′B configuration, the CBM are located at −5.24 eV. For AA′ and AA-SSe, these values are −4.97 and −5.23 eV, respectively. For the AA-SeSe and AA-SS configurations, the CBM is located at −4.54 and −5.08 eV, respectively. Compared with the water redox potentials, they are all just below the reduction potential of $H^+/H_2O$ (−4.44 eV). For the above-mentioned configurations, the CBMs are −6.43 (A′B), −6.35 (AA′), −6.45 (AA-SSe), −6.64 (AA-SeSe), and −7.18 eV (AA-SS), respectively. All of the CBMs are below the oxidation potential of $O_2/H_2O$ (−5.67 eV). This indicates that only the water oxidation reaction is thermodynamically feasible for BL MoSSe, while the water reduction reaction is thermodynamically unfeasible.

We have calculated the work function ($\phi$) by comparing the Fermi energy with the vacuum level ($E_v$). The various *xy*-plane averaged electrostatic potentials and $\phi$ of the BL MoSSe with different geometries are presented in Figure 5. For ML MoSSe, the *xy*-plane averaged electrostatic potential is shown in the Supporting Information, and the corresponding $\phi$ is 6.339 eV, which is bigger than $MoS_2$ (6.11 eV) and $MoSe_2$ (5.49 eV).[69] For BL MoSSe, the *xy*-plane averaged electrostatic potential


DOI: 10.1021/acs.jpcc.8b00257
J. Phys. Chem. C 2018, 122, 6209−6216

curves are not symmetric for the S and Se atoms are out of mirror symmetry of the Mo atoms plane, which is also shown in the ML MoSSe. The corresponding work function is dependent on the stacking orders. For A′B, AA′, and AA-SeSe types, the corresponding $\phi$ values are 6.569, 6.591, and 6.551 eV, respectively. For the AA-SSe type, the corresponding $\phi$ value is 6.351 eV, which is just a little bigger than the ML MoSSe, while, for the AA-SS type, this value is 7.088 eV. Compared with the ML MoSSe, all of the work functions of BL are bigger than ML, suggesting that the electrons should need more energy to be excited to the vacuum level.[70]

**3.5. The Structural and Electronic Properties Dependent on the Thickness of the Janus MoSSe.** The A′B type is the most stable configuration of the BL MoSSe. Therefore, we mainly investigate the A′B configuration for the multilayer MoSSe. The layer of MoSSe is stacked together by van der Waals (vdW) forces, which is similar to graphene, *h*-BN, and other TMDs.[64−68] For $N$ = 3−8, the average $d$ is about 3.13 Å. The average distance between two adjacent layers is about 3.13 Å, and the corresponding $E_b$ values (defined as $E_b = E_{multilayer} - E_{monolayer} \times N$) are −0.360, −0.576, −0.736, −0.954, −1.176, and −1.389 eV, respectively. The optimized geometries are shown in Figure 6a.

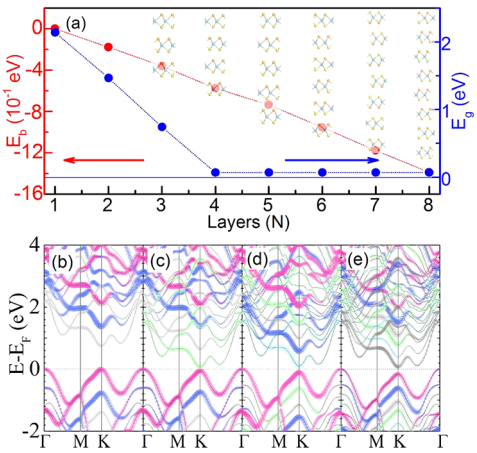


**Figure 6.** (a) Energy difference between the multilayers and monolayer of the MoSSe, with band gap as a function of number of layers ($N$) obtained from DFT-D2 under HSE06 functionals. The inset shows the optimized geometries of multilayers MoSSe with $N$ = 3−8. The band structures of (b) trilayer, (c) four-layer, (d) five-layer, and (e) six-layer MoSSe with AB stacking orders are calculated by the HSE06 functional, respectively. The pink, blue, light gray, light green, light blue, and dark gray lines with dots present the weights of the first, second, third, fourth, fifth, and sixth MoSSe layers, respectively.

For the TMDs, the electronic properties are closely related with the thickness.[55−59,64−68] For monolayer $MoS_2$, it is a direct gap semiconductor. $MoSe_2$, $MoTe_2$, $WS_2$, and $WSe_2$ monolayers are also direct semiconductors.[60,61,63,68] While the thickness increases, BL $MoS_2$, $MoTe_2$, and $WS_2$ all are indirect semiconductors, except for $MoSe_2$.[66] For bulk, they are all indirect semiconductors.[64,66,68] For the multilayer MoSSe, they are also indirect semiconductors. All of the VBM is located at the Γ point, while the CBM is located at the K point. As the thickness increases, the corresponding $E_g$ monotonously decreases for the quantum confinement effect and interaction between the interlayers. The topologies of the band structure of the multilayer MoSSe are quite similar to the ML case, except for the CBM shifted from the original K point to the Γ point.

For the trilayer MoSSe, the corresponding $E_g$ is 0.743 eV. The corresponding VBM is located at the Γ point, while the CBM is still located at the K point, shown in Figure 6b. The corresponding charge density of the valence band (VB) is contributed by the top layer, while the conduction band (CB) is contributed by the bottom layer. This implies that electrons could be directly photoexcited from the top layer to the bottom layer, and leave the holes in the top layer, forming a separated distribution of the electrons and holes, respectively.

When the number of layers $N$ is increased to 4, the corresponding $E_g$ is 0.069 eV. The charge density of VB still comes from the contribution of the top layer, while the CB comes from the contribution of the bottom layer. The charge densities of the bands just below the VB and above the CB at the K point are also composed by the two middle layers, shown in Figure 6c, respectively. For $N$ = 5, the charge density of the band just below the VB at the K point comes from the contribution of the fourth layer. For the bands just above the CB, the second and third layers make the main contribution. For $N$ = 5−8, the corresponding $E_g$ is decreased to 0.069 eV, and the band structures are shown in Figure 6d and e, respectively. Compared with multilayer $MoS_2$,[66] the gap of the multilayer MoSSe decreases much more quickly. This may be caused by the enhanced interaction between the interlayers, quantum confinement, and long-ranged Coulomb effects.[66−68]

In all cases, the VB is composed of the top layer, while the CB is composed of the bottom layer. Other bands near the VB and CB close to the Fermi level at the K point are contributed by the middle layers of the MoSSe.

## CONCLUSIONS

In conclusion, we examine the geometry, electronic, and optical properties of MoSSe with the first-principles calculations. The ML MoSSe is a semiconductor with a direct band gap of 2.14 eV, showing an obvious absorption of the visual light, with suitable band alignment with the water redox potential. The electronic, optical properties, and band alignment of ML MoSSe could be effectively tuned by the biaxial strains, from the direct band gap semiconductor into the indirect one, even metal. The electronic properties and band alignment could also be effectively modulated by the stacking orders and thickness. For BL MoSSe, the most stable A′B configuration is an indirect gap semiconductor. As the thickness increases, the band gap monotonously decreases for the quantum confinement effect and interaction between the layers. The charge densities of VB and CB are always distributed in the top and bottom layers, respectively. The suitable band gap, appropriate band alignment with water redox potential, and notable absorption of the visual light together imply that MoSSe should be a promising candidate for photocatalytic water splitting using solar energy.

## ASSOCIATED CONTENT

### Supporting Information

The Supporting Information is available free of charge on the ACS Publications website at DOI: 10.1021/acs.jpcc.8b00257.

Information on materials, PDOS of ML MoSSe, band structure of ML MoSSe with spin−orbital coupling, band structure under some strains, *xy*-plane averaged electrostatic potential of ML MoSSe, calculated by HSE06, $d_0$



DOI: 10.1021/acs.jpcc.8b00257
J. Phys. Chem. C 2018, 122, 6209−6216

and $E_b$ of other BL MoSSe stacking orders, and the details of the GW-BSE calculation (PDF)

## AUTHOR INFORMATION


### Corresponding Author

*E-mail: zyguan@tsinghua.edu.cn. Phone: +86-010-62772784. Fax: +86-62772784.

### ORCID

Zhaoyong Guan: 0000-0002-6847-5809

Shuanglin Hu: 0000-0001-9729-5500


### Notes

The authors declare no competing financial interest.

## ACKNOWLEDGMENTS

We thank Doctor Xingxing Li and Professor Wenhui Duan for helpful discussions. This work was partially supported by the financial support from the Natural Science Foundation of China (Grant No. 21503201), the President Foundation of China Academy of Engineering Physics (YZJJLX2016004), the National Key Research and Development Program of China (under Grant No. 2016YFB0201203), and Special Program for Applied Research on Super Computation of the NSFC-Guangdong Joint Fund (the second phase) under Grant No. U1501501. The computational resources from Shanghai Supercomputer Center, National supercomputing Centers of Guangzhou, Sunway Taihu Light, and Tsinghua Supercomputer Centers should be acknowledged.

## REFERENCES


(1) Fox, M. A.; Dulay, M. T. Heterogeneous Photocatalysis. *Chem. Rev.* **1993**, *93*, 341−357.

(2) Hoffmann, M. R.; Martin, S. T.; Choi, W. Y.; Bahnemann, D. W. Enviromental Applications of Semiconducutor Photocatalysis. *Chem. Rev.* **1995**, *95*, 69−96.

(3) Linic, S.; Christopher, P.; Ingram, D. B. Plasmonic-metal Nanostructures for Efficient Conversion of Solar to Chemical Energy. *Nat. Mater.* **2011**, *10*, 911−921.

(4) Christoforidis, K. C.; Fornasiero, P. Photocatalytic Hydrogen Production: A Rift into the Future Energy Supply. *ChemCatChem* **2017**, *9*, 1523−1544.

(5) Andoshe, D. M.; Jeon; Jong-Myeong; Kim, Soo Y.; Jang, H. W. Two-Dimensional Transition Metal Dichalcogenide Nanomaterials for Solar Water Splitting. *Electron. Mater. Lett.* **2015**, *11*, 323−335.

(6) Ismail, A. A.; Bahnemann, D. W. Bahnemann. Photochemical Splitting of Water for Hydrogen Production by Photocatalysis: A review. *Sol. Energy Mater. Sol. Cells* **2014**, *128*, 85−101.

(7) Sun, Y. F.; Sun, Z. H.; Gao, S.; Cheng, H.; Liu, Q. H.; Lei, F. C.; Wei, S. Q.; Xie, Y. All-Surface-Atomic-Metal Chalcogenide Sheets for High-Efficiency Visible-Light Photoelectrochemical Water Splitting. *Adv. Energy Mater.* **2014**, *4*, 1300611.

(8) Collins, G.; Armstrong, E.; McNulty, D.; O'Hanlon, S.; Geaney, H.; O'Dwyer, C. 2D and 3D Photonic Crystal Materials for Photocatalysis and Electrochemical Energy Storage and Conversion. *Sci. Technol. Adv. Mater.* **2016**, *17*, 563−582.

(9) Lu, Q. P.; Yu, Y. F.; Ma, Q. L.; Chen, B.; Zhang, H. 2D Transition-Metal-Dichalcogenide-Nanosheet-Based Composites for Photocatalytic and Electrocatalytic Hydrogen Evolution Reactions. *Adv. Mater.* **2016**, *28*, 1917−1933.

(10) Seh, Z. W.; Fredrickson, K. D.; Anasori, B.; Kibsgaard, J.; Strickler, A. L.; Lukatskaya, M. R.; Gogotsi, Y.; Jaramillo, T. F.; Vojvodic, A. Two-Dimensional Molybdenum Carbide (MXene) as an Efficient Electrocatalyst for Hydrogen Evolution. *Acs Energy Letters* **2016**, *1*, 589−594.

(11) Wu, J. J.; Liu, M. J.; Chatterjee, K.; Hackenberg; Ken, P.; Shen, J. F.; Zou, X. L.; Yan, Y.; Gu, J.; Yang, Y. C.; Lou, J.; Ajayan; Pulickel, M. Exfoliated 2D Transition Metal Disulfides for Enhanced Electrocatalysis of Oxygen Evolution Reaction in Acidic Medium. *Adv. Mater. Interfaces* **2016**, *3*, 1500669.

(12) Gao, G.; O'Mullane, A. P.; Du, A. 2D MXenes: A New Family of Promising Catalysts for the Hydrogen Evolution Reaction. *ACS Catal.* **2017**, *7*, 494−500.

(13) Review of Two-dimensional Materials for Photocatalytic Water Splitting from a Theoretical Perspective: Li, Y. G.; Li, Y. L.; Sa, B.; Ahuja, R. *Catal. Sci. Technol.* **2017**, *7*, 545−559.

(14) Ling, C. Y.; Wang, J. Recent Advances in Electrocatalysts for the Hydrogen Evolution Reaction Based on Graphene-Like Two-Dimensional Materials. *Acta Phys.-Chim. Sin.* **2017**, *33*, 869−885.

(15) Wang, Q. H.; Kalantar-Zadeh, K.; Kis, A.; Coleman, J. N.; Strano, M. S. Electronics and Optoelectronics of Two-dimensional Transition Metal Dichalcogenides. *Nat. Nanotechnol.* **2012**, *7*, 699−712.

(16) Bhimanapati, G. R.; Lin, Z.; Meunier, V.; Jung, Y.; Cha, J.; Das, S.; Xiao, D.; Son, Y.; Strano, M. S.; Cooper, V. R.; et al. Recent Advances in Two-Dimensional Materials beyond Graphene. *ACS Nano* **2015**, *9*, 11509−11539.

(17) Zeng, Q. S.; Wang, H.; Fu, W.; Gong, Y. J.; Zhou, W.; Ajayan; Pulickel, M.; Lou, J.; Liu, Z. Band Engineering for Novel Two-Dimensional Atomic Layers. *Small* **2015**, *11*, 1868−1884.

(18) Anasori, B.; Xie, Y.; Beidaghi, M.; Lu, J.; Hosler, B. C.; Hultman, L.; Kent, P. R. C.; Gogotsi, Y.; Barsoum, M. W. Two-Dimensional, Ordered, Double Transition Metals Carbides (MXenes). *ACS Nano* **2015**, *9*, 9507−9516.

(19) Wang, X.; Maeda, K.; Thomas, A.; Takanabe, K.; Xin, G.; Carlsson, M. J.; Domen, K.; Antonietti, M. A Metal-free Polymeric Photocatalyst for Hydrogen Production from Water under Visible Light. *Nat. Mater.* **2009**, *8*, 76−80.

(20) Zhang, Y. J.; Mori, T.; Ye, J. H.; Antonietti, M. Phosphorus-Doped Carbon Nitride Solid: Enhanced Electrical Conductivity and Photocurrent Generation. *J. Am. Chem. Soc.* **2010**, *132*, 6294−6295.

(21) Mahmood, J.; Lee, E. K.; Jung, M.; Shin, D.; Jeon, I.-Y.; Jung, S.-M.; Choi, H.-J.; Seo, J.-M.; Bae, S.-Y.; Sohn, S.-D.; et al. Nitrogenated Holey Two-Dimensional Structures. *Nat. Commun.* **2015**, *6*, 6486−6492.

(22) Lu, A. Y.; Zhu, H. Y.; Xiao, J.; Chuu, C.-P.; Han, Y.; Chiu, M.-H.; Cheng, C.-C.; Yang, C.-W.; Wei, K.-H.; Yang, Y. M.; et al. Janus Monolayers of Transition Metal Dichalcogenides. *Nat. Nanotechnol.* **2017**, *12*, 744−749.

(23) Zhang, J.; Jia, S.; Kholmanov, I.; Dong, L.; Er, D. Q.; Chen, W. B.; Guo, H.; Jin, Z. H.; Shenoy; Vivek, B.; Shi, L.; Lou, J. Janus Monolayer Transition-Metal Dichalcogenides. *ACS Nano* **2017**, *11*, 8192−8198.

(24) Boker, T.; Severin, R.; Muller, A.; Janowitz, C.; Manzke, R.; Voss, D.; Kruger, P.; Mazur, A.; Pollmann, J. Band Structure of $MoS_2$, $MoSe_2$, and alpha-$MoTe_2$: Angle-resolved Photoelectron Spectroscopy and ab initio Calculations. *Phys. Rev. B: Condens. Matter Mater. Phys.* **2001**, *64*, 235305.

(25) Cheng, Y. C.; Zhu, Z. Y.; Tahir, M.; Schwingenschlögl, U. Spin-Orbit-Induced Spin Splittings in Polar Transition Metal Dichalcogenide Monolayers. *EPL* **2013**, *102*, 57001.

(26) Dong, L.; Lou, J.; Shenoy, V. B. Large In-Plane and Vertical Piezoelectricity in Janus Transition Metal Dichalchogenides. *ACS Nano* **2017**, *11*, 8242−8248.

(27) Cheiwchanchamnangij, T.; Lambrecht, W. R. L. Quasiparticle Band Structure Calculation of Monolayer, Bilayer, and Bulk $MoS_2$. *Phys. Rev. B: Condens. Matter Mater. Phys.* **2012**, *85*, 205302.

(28) Ramasubramaniam, A. Large Excitonic Effects in Monolayers of Molybdenum and Tungsten Dichalcogenides. *Phys. Rev. B: Condens. Matter Mater. Phys.* **2012**, *86*, 115409.

(29) Grimme, S. Semiempirical GGA-Type Density Functional Constructedwith a Long-Range Dispersion Correction. *J. Comput. Chem.* **2006**, *27*, 1787−1799.

(30) Dion, M.; Rydberg, H.; Schröder, E.; Langreth, D. C.; Lundqvist, B. I. Van der Waals Density Functional for General Geometries. *Phys. Rev. Lett.* **2004**, *92*, 246401.




DOI: 10.1021/acs.jpcc.8b00257
J. Phys. Chem. C 2018, 122, 6209−6216

(31) Thonhauser, T.; Cooper, V. R.; Shen, L.; Puzder, A.; Hyldgaard, P.; Langreth, D. C. Van der Waals Density Functional: Self-consistent Potential and the Nature of the van der Waals Bond. *Phys. Rev. B: Condens. Matter Mater. Phys.* **2007**, *76*, 125112.
(32) Klimeš, J.; Bowler, D. R.; Michaelides, A. J. Chemical Accuracy for the van der Waals Density Functional. *J. Phys.: Condens. Matter* **2010**, *22*, 022201.
(33) Tkatchenko, A.; Scheffler, M. Accurate Molecular Van Der Waals Interactions from Ground-State Electron Density and Free-Atom Reference Data. *Phys. Rev. Lett.* **2009**, *102*, 073005.
(34) Tkatchenko, A.; DiStasio, R. A.; Car, R.; Scheffler, M. Accurate and Efficient Method for Many-Body van der Waals Interactions. *Phys. Rev. Lett.* **2012**, *108*, 236402.
(35) Heyd, J.; Scuseria, G. E.; Ernzerhof, M. Hybrid Functionals Based on a Screened Coulomb Potential (vol 118, pg 8207, 2003). *J. Chem. Phys.* **2003**, *118*, 8207.
(36) Heyd, J.; Scuseria, G. E.; Ernzerhof, M. Hybrid Functionals Based on a Screened Coulomb Potential. *J. Chem. Phys.* **2006**, *124*, 219906.
(37) Hybertsen, M. S.; Louie, S. G. Electron Correlation in Semiconductors and Insulators: Band Gaps and Quasiparticle. *Phys. Rev. B: Condens. Matter Mater. Phys.* **1986**, *34*, 5390.
(38) Shishkin, M.; Kresse, G. Implementation and Performance of the Frequency-dependent GW Method within the PAW Framework. *Phys. Rev. B: Condens. Matter Mater. Phys.* **2006**, *74*, 035101.
(39) Shishkin, M.; Kresse, G. Self-consistent *GW* Calculations for Semiconductors and Insulators. *Phys. Rev. B: Condens. Matter Mater. Phys.* **2007**, *75*, 235102.
(40) Fuchs, F.; Furthmüller, J.; Bechstedt, F.; Shishkin, M.; Kresse, G. Quasiparticle Band Structure Based on a Generalized Kohn-Sham Scheme. *Phys. Rev. B: Condens. Matter Mater. Phys.* **2007**, *76*, 115109.
(41) Shishkin, M.; Marsman, M.; Kresse, G. Accurate Quasiparticle Spectra from Self-Consistent *GW* Calculations with Vertex Corrections. *Phys. Rev. Lett.* **2007**, *99*, 246403.
(42) Albrecht, S.; Reining, L.; Del Sole, R.; Onida, G. Ab Initio Calculation of Excitonic Effects in the Optical Spectra of Semiconductors. *Phys. Rev. Lett.* **1998**, *80*, 4510.
(43) Rohlfing, M.; Louie, S. G. Electron-Hole Excitations in Semiconductors and Insulators. *Phys. Rev. Lett.* **1998**, *81*, 2312.
(44) Kresse, G.; Furthmüller, J. Efficiency of Ab-Initio Total Energy Calculations for Metals and Semiconductors Using a Plane-Wave Basis Set. *Comput. Mater. Sci.* **1996**, *6*, 15−50.
(45) Kresse, G. Efficient Iterative Schemes for Ab Initio Total-Energy Calculations Using a Plane-Wave Basis Set. *Phys. Rev. B: Condens. Matter Mater. Phys.* **1996**, *54*, 11169−11186.
(46) Perdew, J. P.; Burke, K.; Ernzerhof, M. of Physics. D. Generalized Gradient Approximation Made Simple. *Phys. Rev. Lett.* **1996**, *77*, 3865−3868.
(47) Guan, Z. Y.; Ni, S.; Hu, S. L. Band Gap Opening of Graphene by Forming Graphene/$PtSe_2$ van der Waals Heterojunction. *RSC Adv.* **2017**, *7*, 45393−45399.
(48) Guan, Z. Y.; Lian, C. S.; Hu, S. L.; Ni, S.; Li, J.; Duan, W. H. Tunable Structural, Electronic, and Optical Properties of Layered Two-Dimensional $C_2N$ and $MoS_2$ van der Waals Heterostructure as Photovoltaic Material. *J. Phys. Chem. C* **2017**, *121*, 3654−3660.
(49) Baskin, Y.; Meyer, L. Lattice Constants of Graphite at Low Temperatures. *Phys. Rev.* **1955**, *100*, 544.
(50) Zacharia, R.; Ulbricht, H.; Hertel, T. Interlayer Cohesive Energy of Graphite from Thermal Desorption of Polyaromatic Hydrocarbons. *Phys. Rev. B: Condens. Matter Mater. Phys.* **2004**, *69*, 1−7.
(51) Geim, A. K.; Novoselov, K. S. The Rise of Graphene. *Nat. Mater.* **2007**, *6*, 183−191.
(52) Monkhorst, J. H.; Park, D. J. Special Points for Brilouin-zone Interation. *Phys. Rev. B: Condens. Matter Mater. Phys.* **1976**, *13*, 5188.
(53) Gajdoš, M.; Hummer, K.; Kress, G.; Furthmüller, J.; Bechstedt, F. Linear Optical Properties in the Projector-Augmented Wave Methodology. *Phys. Rev. B: Condens. Matter Mater. Phys.* **2006**, *73*, 045112.
(54) Gai, Y. Q.; Li, J. B.; Li, S. S.; Xia, J. B.; Wei, S. H. Design of Narrow-Gap $TiO_2$: A Passivated Codoping Approach for Enhanced Photoelectrochemical Activity. *Phys. Rev. Lett.* **2009**, *102*, 036402.
(55) Geim, A. K.; Grigorieva, I. V. Van der Waals heterostructures. *Nature* **2013**, *499*, 419−425.
(56) Novoselov, K. S.; Mishchenko, A.; Carvalho, A.; Castro Neto, A. H. 2D materials and van der Waals heterostructures. *Science* **2016**, *353*, aac9439.
(57) Liu, Y.; Weiss, N. O.; Duan, X. D.; Cheng, H. C.; Huang, X.; Duan, X. F. Van der Waals Heterostructures and Devices. *Nature. Review. Materials* **2016**, *1*, 16042.
(58) Jariwala, D.; Marks, T. J.; Hersam, M. C. Mixed-dimensional van der Waals Heterostructures. *Nat. Mater.* **2017**, *16*, 170−181.
(59) Xia, W. S.; Dai, L. P.; Yu, P.; Tong, X.; Song, W. P.; Zhang, G. J.; Wang, Z. M. Recent Progress in van der Waals Heterojunctions. *Nanoscale* **2017**, *9*, 4324−4365.
(60) Chang, C. H.; Fan, X. F.; Lin, S. H.; Kuo, J. L. Orbital Analysis of Electronic Structure and Phonon Dispersion in $MoS_2$, $MoSe_2$, $WS_2$, and $WSe_2$ Monolayers under Strain. *Phys. Rev. B: Condens. Matter Mater. Phys.* **2013**, *88*, 195420.
(61) Conley, H. J.; Wang, B.; Ziegler, J. I.; Haglund, R. F.; Pantelides, S. T.; Bolotin, K. L. Bandgap Engineering of Strained Monolayer and Bilayer $MoS_2$. *Nano Lett.* **2013**, *13*, 3626−3630.
(62) Wu, W. Z.; Wang, L.; Li, Y. L.; Zhang, F.; Lin, L.; Niu, S. M.; Chenet, D.; Zhang, X.; Hao, Y. F.; Heinz, T. F. Piezoelectricity of Single-atomic-layer $MoS_2$ for Energy Conversion and Piezotronics. *Nature* **2014**, *514*, 470.
(63) Scalise, E.; Houssa, M.; Pourtois, G.; Afanas'ev, V. V. Stesmans. First-principles Study of Strained 2D $MoS_2$. *Phys. E* **2014**, *56*, 416−421.
(64) Mak, K. F.; Lee, C.; Hone, J.; Shan, J.; Heinz, T. F. Atomically Thin $MoS_2$: A New Direct-Gap Semiconductor. *Phys. Rev. Lett.* **2010**, *105*, 136805.
(65) He, J. G.; Hummer, K.; Franchini, C. Stacking Effects on the Electronic and Optical Properties of Bilayer Transition Metal Dichalcogenides $MoS_2$, $MoSe_2$, $WS_2$, and $WSe_2$. *Phys. Rev. B: Condens. Matter Mater. Phys.* **2014**, *89*, 075409.
(66) Yun, W. S.; Han, S. W.; Hong, S. C.; Kim, I. G.; Lee, J. D. Thickness and Strain Effects on Electronic Structures of Transition Metal Dichalcogenides: 2H-$MX_2$ Semiconductors (M = Mo, W; X = S, Se, Te). *Phys. Rev. B: Condens. Matter Mater. Phys.* **2012**, *85*, 033305.
(67) Butler, S. Z.; Hollen, S. M.; Cao, L. Y.; Cui, Y.; Gupta, J. A.; Gutierrez, H. R.; Heinz, T. F.; Hong, S. S.; Huang, J. X.; Ismach, A. F.; et al. Progress, Challenges, and Opportunities in Two-Dimensional Materials Beyond Graphene. *ACS Nano* **2013**, *7*, 2898−2926.
(68) Xu, M. S.; Liang, T.; Shi, M. M.; Chen, H. Z. Graphene-Like Two-Dimensional Materials. *Chem. Rev.* **2013**, *113*, 3766−3798.
(69) Lanzillo, N. A.; Simbeck, A. J.; Nayak, S. K. Strain Engineering the Work Function in Monolayer Metal Dichalcogenides. *J. Phys.: Condens. Matter* **2015**, *27*, 175501.
(70) Jin, H. J.; Yoon, W. Y.; Jo, W. Control of Work Function of $MoS_2$ with Ferroelectric Polarization in Honeycomb-like Heterostructure. *Appl. Phys. Lett.* **2017**, *110*, 191601.


DOI: 10.1021/acs.jpcc.8b00257
*J. Phys. Chem. C* 2018, 122, 6209−6216